JOURNAL OF GEOPHYSICAL RESEARCH, VOL. 89, NO. B13, PAGES 11,476-11,494, DECEMBER 10, 1984

RAYLEIGH WAVE SCATTERING AT A BASIN TYPE HETEROGENEITY

Rüdiger Szelwis

Institut für Geophysik, Universität Hamburg, Federal Republic of Germany

Abstract. Rayleigh waves are investigated numerically on a subsurface model composed of a layer over a substratum, and a basin embedded in the layer. The basin elastic parameters are varied to obtain three laterally heterogeneous models of different velocity contrast between the basin and the layer. The wave incident upon the basin is defined to be a pure fundamental mode having wavelengths comparable to the basin dimensions. Analysis of the wave transmitted reveals mode conversion, i.e., higher mode excitation which is increasingly important with increased velocity contrast. In terms of (rate of transport of) energy, the contribution of the first higher mode (being the only higher mode in the analysis interval) is relatively small, which differs from earlier results for the case of Love waves. To enable direct comparison, a fundamental Love mode having spectral properties analogous to the Rayleigh wave, is propagated across the subsurface models of the present paper. Hence, the discrepancy between the two waves basically arises from the structure of the subsurface transfer functions. The fraction of modal energy transmitted across the basin proves a sensitive indicator of the velocity contrast, showing similarity in amount and frequency dependence for Rayleigh and Love waves. In terms of modal amplitudes, conventionally considered in practice, the first higher mode contribution (due to mode conversion) is roughly comparable to the fundamental mode contribution, for both transmitted waves. It implies that the amplitude spectrum of the transmitted surface wave is modulated in the horizontal direction. The effect adds to the spectral distortion due to reflection at the basin. Hence, standard interpretation based upon a laterally homogeneous model, of measurements in corresponding regions, may be significantly biased.

Introduction

Surface waves have been applied to investigations of the crustal structure and of shallow earthquakes. Numerous investigations have inverted the dispersion information to yield the velocity distribution with depth. More recently, anelasticity and earthquake source parameters have been determined by inversion of the amplitude information over an extended frequency range.

Tsai and Aki [1970] have developed a method of using surface wave spectra from shallow earthquakes for focal depth determination. Observed amplitude spectra were explained in terms of a point force system located at different depths of a layered model. The results agreed with findings from body wave travel times. Effects of scattering due to lateral heterogeneities or of attenuation due to anelasticity were neglected. A more detailed knowledge of the propagation effects would have permitted the seismic moment in addition to the focal depth. Cheng and Mitchell [1981] have used the shape of Rayleigh wave amplitude spectra for inversion of crustal Q structure. Mode spectra obtained from relatively short wave paths in the United States, were explained in terms of a layer (corresponding to the upper crust) over a substratum. Kijko and Mitchell [1983] have applied the method in the Barents shelf region. Again, the observations were explained by means of a two-layer crustal model. A higher resolution was not possible due to uncertainties in the source parameters and the effects of lateral heterogeneities along the path of propagation.

These examples demonstrate the restrictions of surface wave interpretation in terms of the classical plane-layered model, and the need for quantitative evidence about scattering due to near-surface lateral heterogeneities. At present, scattering of surface waves is not well known. Theoretical approaches are difficult, and have been confined to highly idealized models. Bukchin and Levshin [1980] have obtained an approximate solution to the propagation of Love waves across a vertical discontinuity by application of the Green's function technique. Their method overcomes the usual restriction that the waves transmitted and reflected can be described completely by superposition of normal modes. For a step-like increase in thickness of a two-layer model, it was found that (i) the amplitude ratio between transmitted body waves and surface waves is about one tenth; (ii) the amplitudes of reflected body waves and surface waves are comparable, and about one sixth of the amplitudes of the incident Love wave.

Numerical approaches (finite differences or finite elements) to scattering become increasingly important due to a relatively simple algorithm, great flexibility, and accuracy. A disadvantage is the high amount of computer storage capacity and of computation time required for the accurate modeling of realistic problems. Numerical methods are therefore especially useful in problems of scattering at heterogeneities having dimensions of the order of the wavelengths. In this paper, wave propagation is modeled using finite differences (FD). A discussion of finite difference methods (homogeneous and heterogeneous formulations) for seismic waves has been given by Boore [1972]. In his Ph.D. thesis, Boore [1970] has investigated Love wave propagation across a local heterogeneity of a plane-layered medium. The wave was defined analytically in terms of the eigenfunctions of the layering, and was used to start the finite difference solution to the problem. The approach has since been adopted by a number of authors. Usually, interpretation refers to the spatial

Paper number 4B1126.
0148-0227/84/004B-1126$05.00

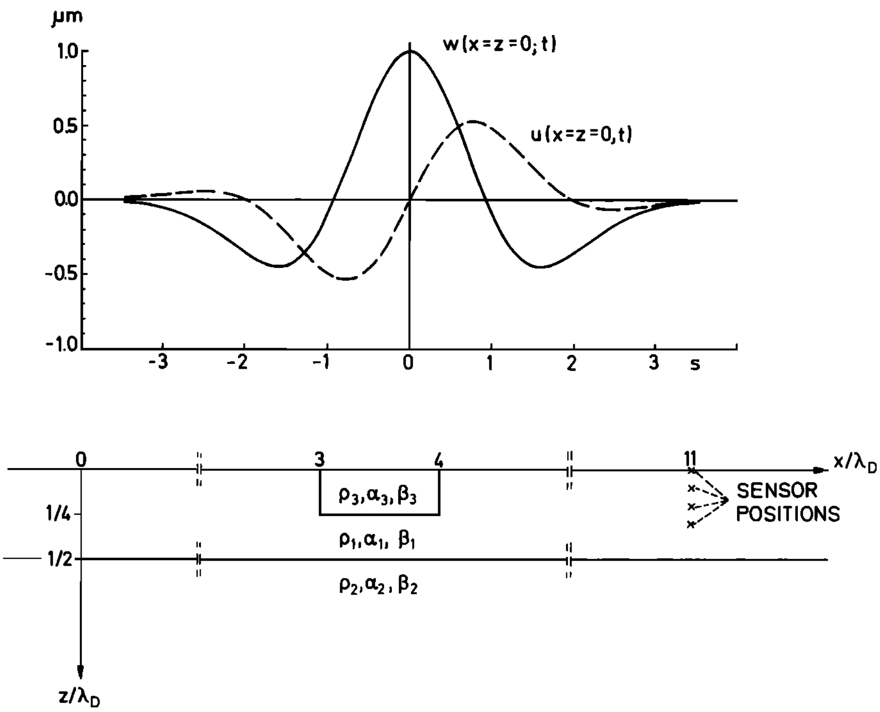

Fig. 1. (Upper part) Seismograms of the fundamental Rayleigh mode at the coordinate origin. The vertical component of displacement w(t) is defined by a Ricker wavelet, which implies the corresponding horizontal component u(t). (Lower part) Subsurface elastic model. Density, compressional wave velocity, and shear wave velocity of the layering are given by ρ_1=2.6 g/cm^3, α_1=4.5 km/s, β_1=2.45 km/s and ρ_2=2.8 g/cm^3, α_2= 6.0 km/s, β_2=3.45 km/s. The basin parameters take on different values to define three laterally heterogeneous models (see Table 1). The model dimensions are scaled by the dominant wavelength λ_D=10 km.

waveform. Fuyuki and Matsumoto [1980], for example, have determined Rayleigh wave transmission and reflection properties at a trench of a homogeneous halfspace, by analysis of the surface displacements at a fixed time.

The author has presented a hybrid approach to surface wave transmission across a local heterogeneity, based upon seismogram frequency spectra of the incident wave and of the wave transmitted [Szelwis, 1983]. The method has been applied to Love waves on a layered model involving a sedimentary basin. The present paper considers Rayleigh waves, and also compares the transmission properties of the two waves.

Analytical Definition of the Incident Wave

Free surface waves of a laterally homogeneous waveguide are interpretable by mode contributions. In the case of a two-dimensional elastic medium, horizontal and vertical components of Rayleigh wave displacement, u and w, may be represented by

$$\begin{Bmatrix} u(x,z,t) \\ w(x,z,t) \end{Bmatrix} = \frac{1}{2\pi}\int_{-\infty}^{\infty} \exp(-i\omega t) \cdot \sum_n \begin{Bmatrix} U^{(n)}(x,z,\omega) \\ W^{(n)}(x,z,\omega) \end{Bmatrix} d\omega \quad (1a)$$

where

$$\begin{Bmatrix} U^{(n)}(x,z,\omega) \\ W^{(n)}(x,z,\omega) \end{Bmatrix} = \alpha^{(n)}(\omega) \begin{Bmatrix} T_H^{(n)}(z,\omega) \\ T_V^{(n)}(z,\omega) \end{Bmatrix} \cdot \exp(i\omega x/c^{(n)}) \quad (1b)$$

The Cartesian coordinates x,z refer to the origin at the surface of the medium; x is parallel to and positive in the direction of propagation, and z is vertical and positive downward. The time-frequency (t-ω) Fourier transforms of the modal components, $U^{(n)}$ and $W^{(n)}$ (n is the mode index), are composed of (1) horizontal transfer function $\exp(i\omega x/c^{(n)})$, where $c^{(n)}$ is the phase velocity, (2) vertical transfer function $T_H^{(n)}$ or $T_V^{(n)}$ for the horizontal or vertical displacement component, and (3) mode coefficient $\alpha^{(n)}$.

Accordingly, a free Rayleigh wave propagating in a waveguide of known properties, is completely determined by $\alpha^{(n)}(\omega)$. If there is only one mode, the wave is completely determined by a single (horizontal or vertical component) seismogram. The wave incident upon the heterogeneity is defined to be purely fundamental mode:

$$\alpha^{(n)}(\omega) = \alpha^{(1)}(\omega)\ \delta_{n1} \quad (2)$$

where δ is Kronecker's delta.

Assume the vertical component seismogram $w_0(t)$

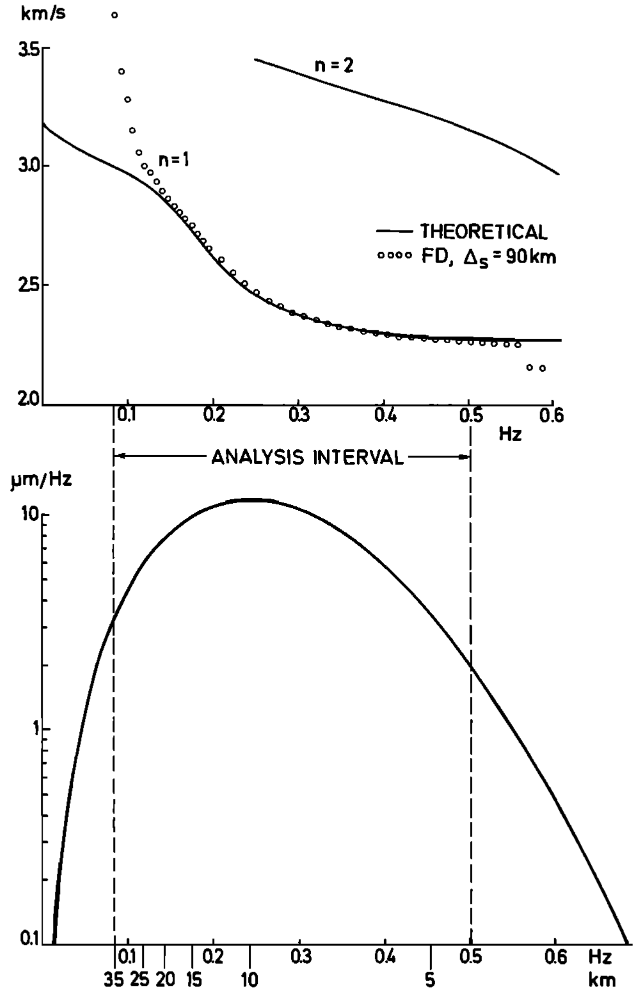

Fig. 2. (Upper part) Phase velocity of the laterally homogeneous layering (model M1). Comparison between theoretical velocity and FD velocity computed from two surface seismograms separated by 90 km. (Lower part) Amplitude spectrum of w(t) (Figure 1), dependent upon frequency or fundamental mode wavelength.

to be known at the coordinate origin. Then, comparing expression

$$w(t;x=z=0) \equiv w_0(t) = \frac{1}{2\pi}\int_{-\infty}^{\infty} \cdot \exp(-i\omega t)\, W_0(\omega)\, d\omega \qquad (3)$$

($W_0(\omega)$ is the Fourier frequency spectrum of $w_0(t)$), to (1a) and (1b) and taking into account (2), it follows that the incident wave is given by

$$\begin{Bmatrix} U_A(x,z,\omega) \\ W_A(x,z,\omega) \end{Bmatrix} = \frac{W_0(\omega)}{T_V^{(1)}(0,\omega)} \cdot \begin{Bmatrix} T_H^{(1)}(z,\omega) \\ T_V^{(1)}(z,\omega) \end{Bmatrix} \exp(i\omega x/c^{(1)}) \qquad (4)$$

where the index A denotes "analytical wave."

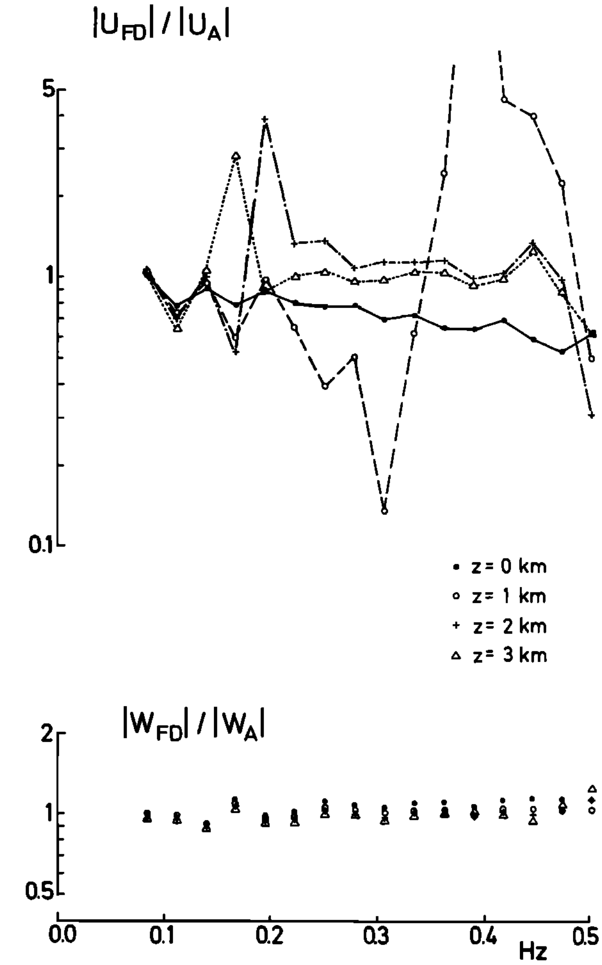

Fig. 3a. Model M1. Amplitude ratio at the vertical array of sensors (Figure 1), obtained by numerical propagation (index FD) and by analytical propagation (index A) of the fundamental mode. (Upper part) horizontal component and (lower part) vertical component.

For convenience of notation, the vertical transfer functions $T_H^{(n)}$, $T_V^{(n)}$ are normalized by $T_V^{(1)}(0,\omega)$ to yield

$$\begin{Bmatrix} \tilde{T}_H^{(n)}(z,\omega) \\ \tilde{T}_V^{(n)}(z,\omega) \end{Bmatrix} = \frac{1}{T_V^{(1)}(0,\omega)} \cdot \begin{Bmatrix} T_H^{(n)}(z,\omega) \\ T_V^{(n)}(z,\omega) \end{Bmatrix} \qquad (5a)$$

Correspondingly, the mode coefficients are redefined by

$$A^{(n)}(\omega) = T_V^{(1)}(0,\omega)\, \alpha^{(n)}(\omega) \qquad (5b)$$

allowing direct comparison with $W_0(\omega)$.

Now, the frequency-time (inverse) Fourier transform of (4) gives the fundamental mode displacement field at every point of the waveguide as a function of time. Direct numerical computation of the wave field on a (two-dimensional) spatial grid requires a Fourier transform at

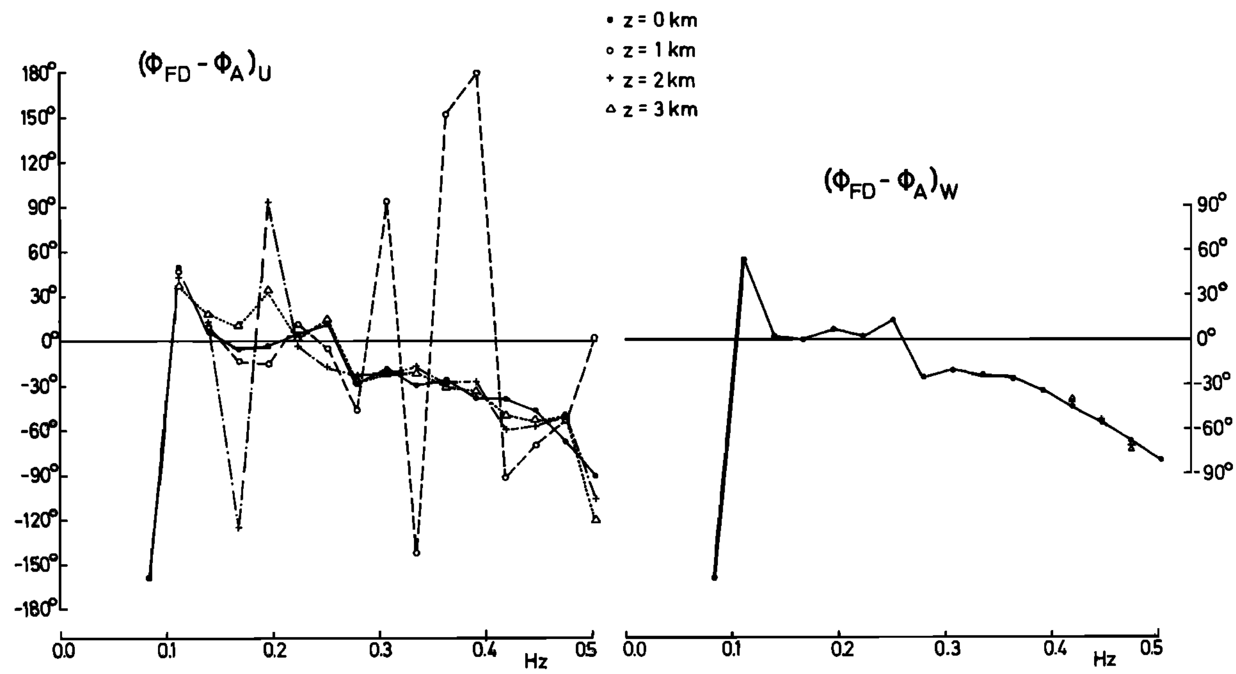

Fig. 3b. Model M1. Phase difference at the sensor array, between the fundamental mode propagated numerically (index FD) and analytically (index A). (Left) horizontal component and (right) vertical component.

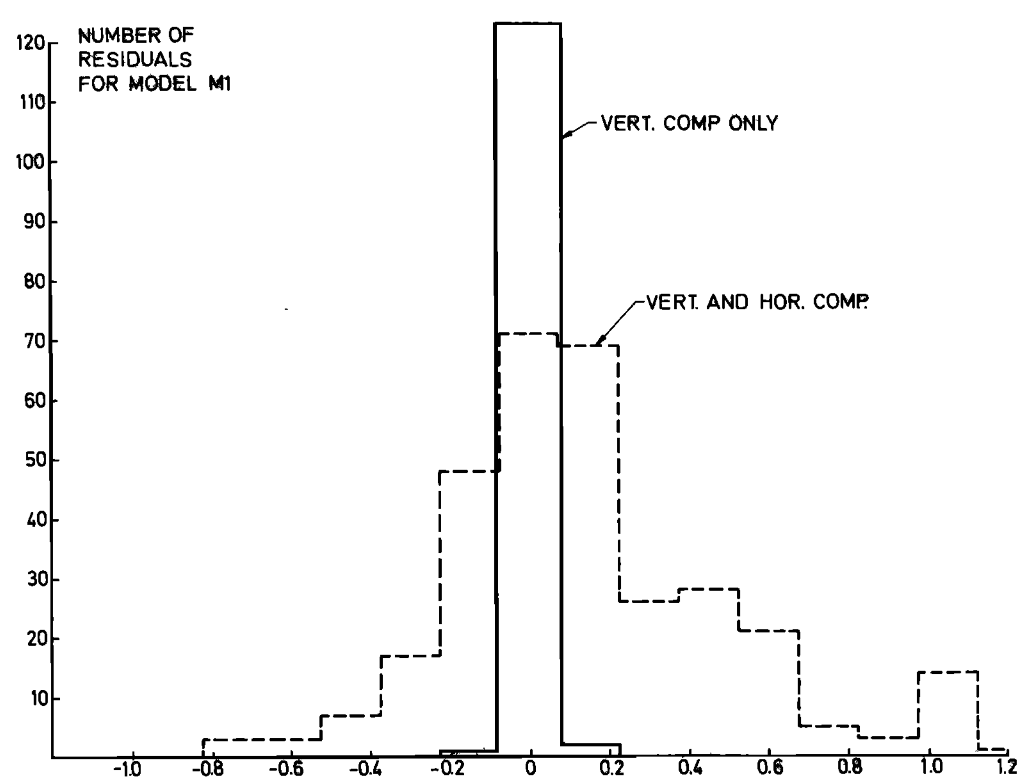

Fig. 4a. Model M1. Histograms of residuals due to inversion of both horizontal and vertical components, and of the vertical component only.

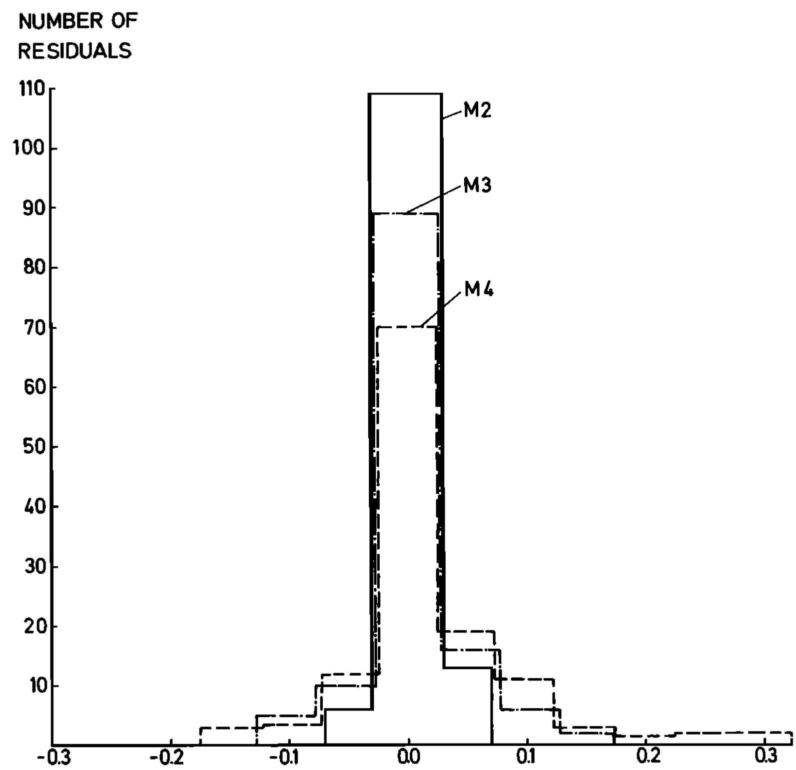

Fig. 4b. Histograms of residuals due to inversion of the vertical component of motion, for the three laterally heterogeneous subsurface models.

every grid point, which is generally not feasible. A more useful form is obtained by transforming from frequency ω to wavenumber k associated with the direction of propagation x. This yields the following representation:

$$\begin{Bmatrix} u_A(x,z,t) \\ w_A(x,z,t) \end{Bmatrix} = \int_{-\infty}^{\infty} \exp(ikx)\, \frac{\hat{W}(k)}{2\pi} \cdot \begin{Bmatrix} \tilde{T}_H^{(1)}(z,k) \\ \tilde{T}_V^{(1)}(z,k) \end{Bmatrix} \exp(-ikc^{(1)}t)\, dk \tag{6a}$$

where

$$\hat{W}(k) = \frac{d\omega^{(1)}}{dk} W_0(\omega^{(1)}) \tag{6b}$$

Computation of the spatial displacement field according to (6a) and (6b) requires one Fourier transform at every depth level of the grid.

FD Wave Propagation

The equations of motion governing the propagation of free Rayleigh waves in a two-dimensional heterogeneous elastic medium are given by

$$\rho\frac{\partial^2 u}{\partial t^2} = \frac{\partial}{\partial x}(D + 2E) + \frac{\partial G}{\partial z}$$
$$\rho\frac{\partial^2 w}{\partial t^2} = \frac{\partial}{\partial z}(D + 2F) + \frac{\partial G}{\partial x} \tag{7}$$

where

$$D = \lambda\left(\frac{\partial u}{\partial x} + \frac{\partial w}{\partial z}\right) \qquad E = \mu\frac{\partial u}{\partial x}$$

$$G = \mu\left(\frac{\partial u}{\partial z} + \frac{\partial w}{\partial x}\right) \qquad F = \mu\frac{\partial w}{\partial x}$$

and where the density ρ and Lamé's parameters λ and μ are functions of the spatial coordinates x, z.

The second order partial differential equations (7) are solved by the heterogeneous finite difference formulation. Approximations to the differentials are analogous to those of Kelly et al. [1976], except that the density ρ is considered here to be spatially variable. Hence the two coupled FD equations corresponding to (7) differ from those of Kelly et al. by explicit occurrence of λ, μ, and ρ.

Conformable to standard procedure, the free surface boundary conditions, i.e., vanishing of normal and tangential stress components, are treated explicitly to specify the displacement at artificial grid points exterior to the medium of propagation. Boundary conditions at a discontinuity within the medium are involved in the heterogeneous FD formulation. Initial conditions are defined by the fundamental mode displacements at two points in time separated by the numerical time increment.

A stability condition for the FD forward time differencing scheme on a regular two-dimensional spatial grid is given by

$$\Delta t \le \Delta r/(\alpha_m^2 + \beta_m^2)^{1/2}$$

where Δt represents the time increment, Δr is the grid interval, and α_m and β_m are maximum compressional and shear wave velocities occurring in the model. The existence of stability implies convergence for all practical purposes [Boore, 1972].

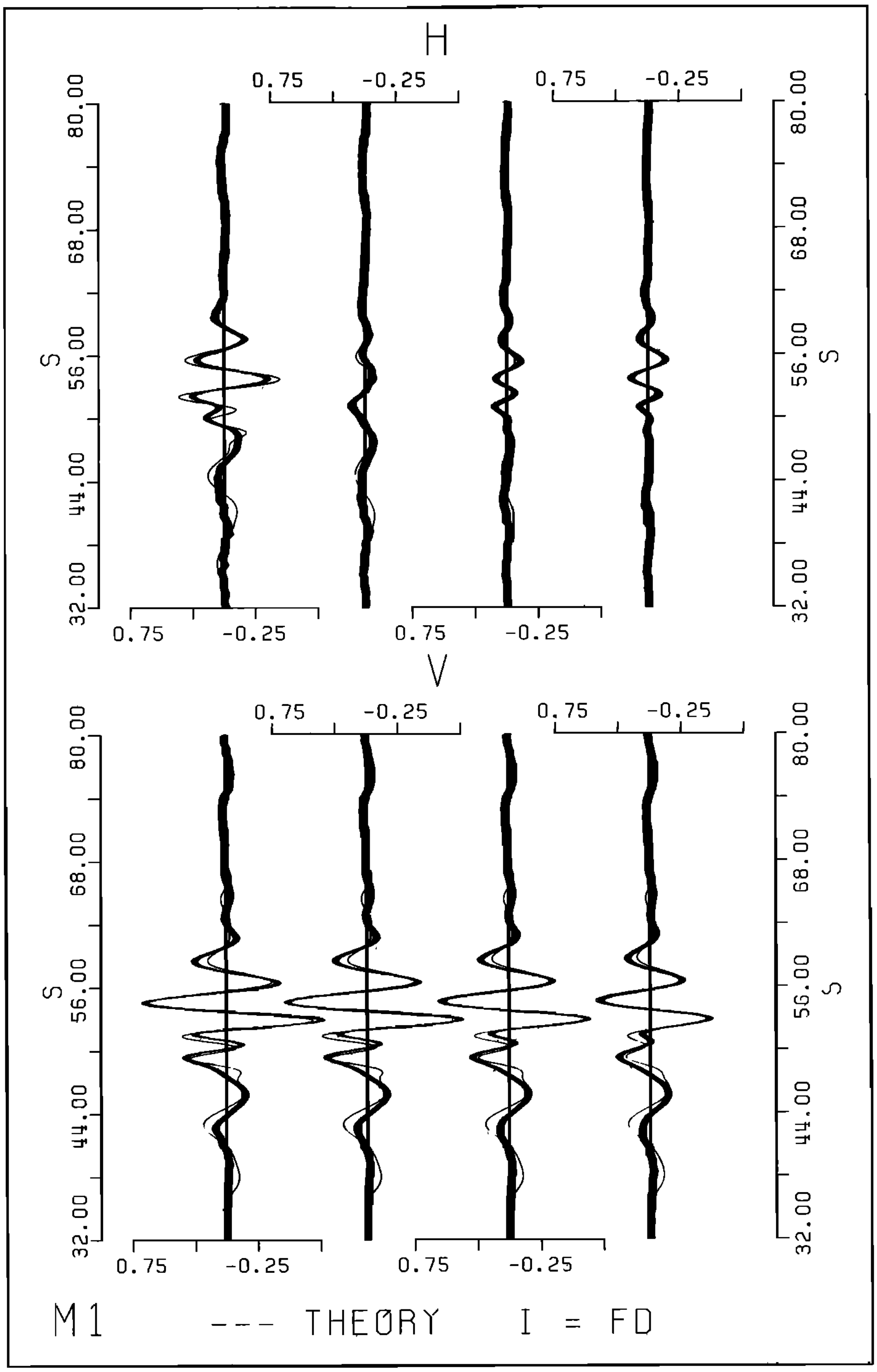

Fig. 5a. Model M1. Seismograms at the sensor array, obtained by analytical propagation and by numerical propagation of the fundamental mode. The analytical seismograms are given by a thin line, and the FD seismograms by vertical bars simulating a relatively broad line. From left to right, the seismograms correspond to increasing depth. The time scale is in seconds, and the amplitude scale is in μm. (Upper part) horizontal component and (lower part) vertical component.

Wave propagation on a lattice is known to be subject to "grid dispersion." According to Alford et al. [1974], the effect is important if there are less than about 10 grid points per wavelength, and tends to become more pronounced as the distance the wave has travelled through the grid increases.

In this paper, Δr = 0.5 km, and Δt = 0.07 s which is 3% below the stability limit. The amplitude spectrum of the analytical wave--represented by a Ricker transient--is maximal at a (fundamental mode) wavelength of 20 Δr, and assumes half the maximum value at wavelengths of about 50 Δr and 12 Δr (Figure 2).

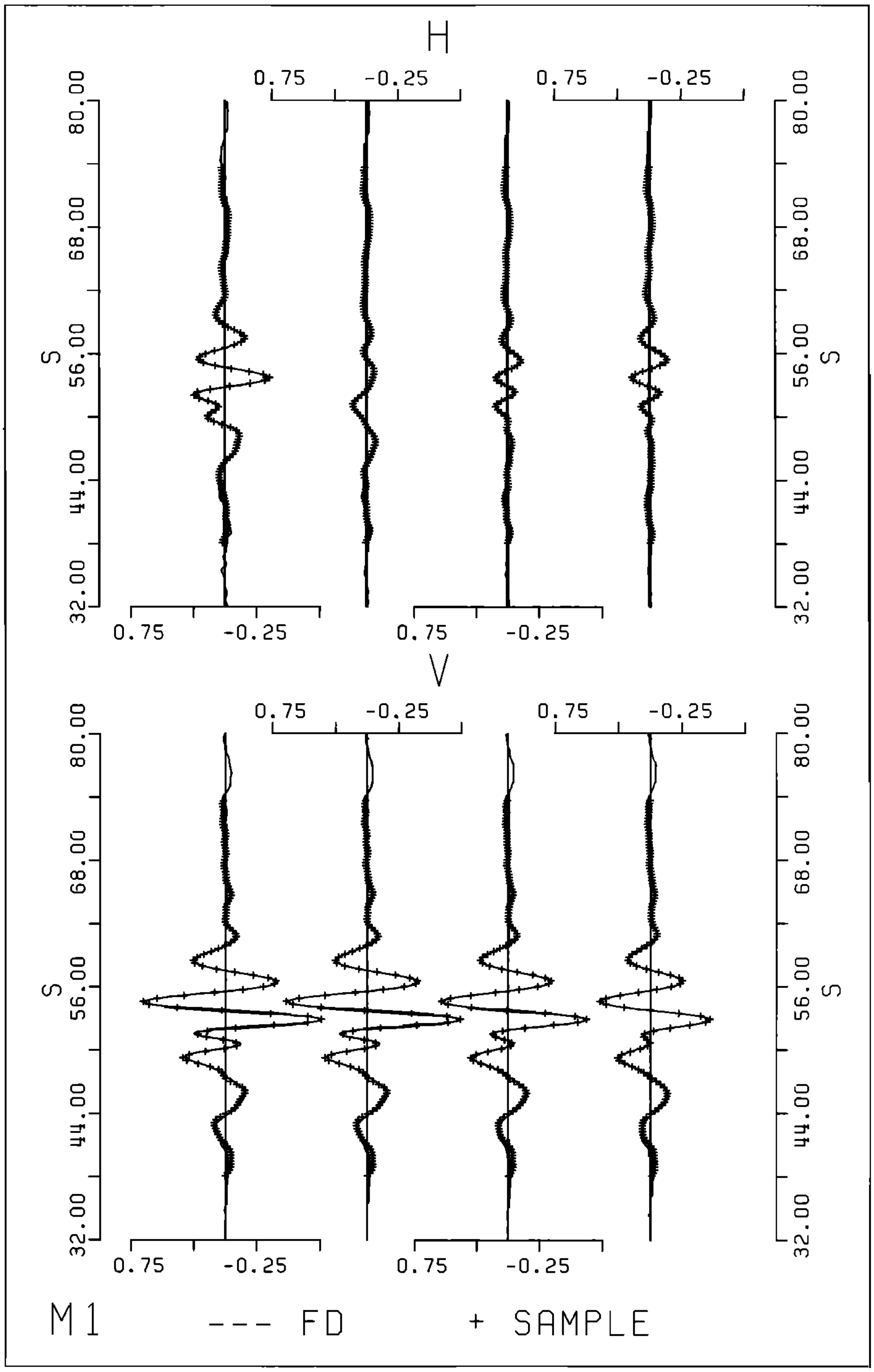

Fig. 5b. Model M1. Seismograms at the sensor array. Comparison between FD seismograms and "observational" seismograms, represented by a continuous line and by crosses, respectively. For legend, see Figure 5a.

Inversion

Propagation of the Rayleigh wave across the heterogeneous region is subject to elastic scattering which generally implies mode conversion, i.e., excitation of trapped higher modes, and also conversion into leaky modes and body waves. The relative importance of these effects depends upon geometrical and scale parameters (for example, depth location and size of the heterogeneity relative to the wavelengths) as well as material properties (for example, the impedance contrast represented by the heterogeneity). This paper considers a local heterogeneity of the form of a basin, the lateral and vertical dimensions of which correspond to the dominant wavelength and to a quarter of the dominant wavelength, respectively (Figure 1). The elastic parameters of the basin are varied to yield different velocity (or impedance)

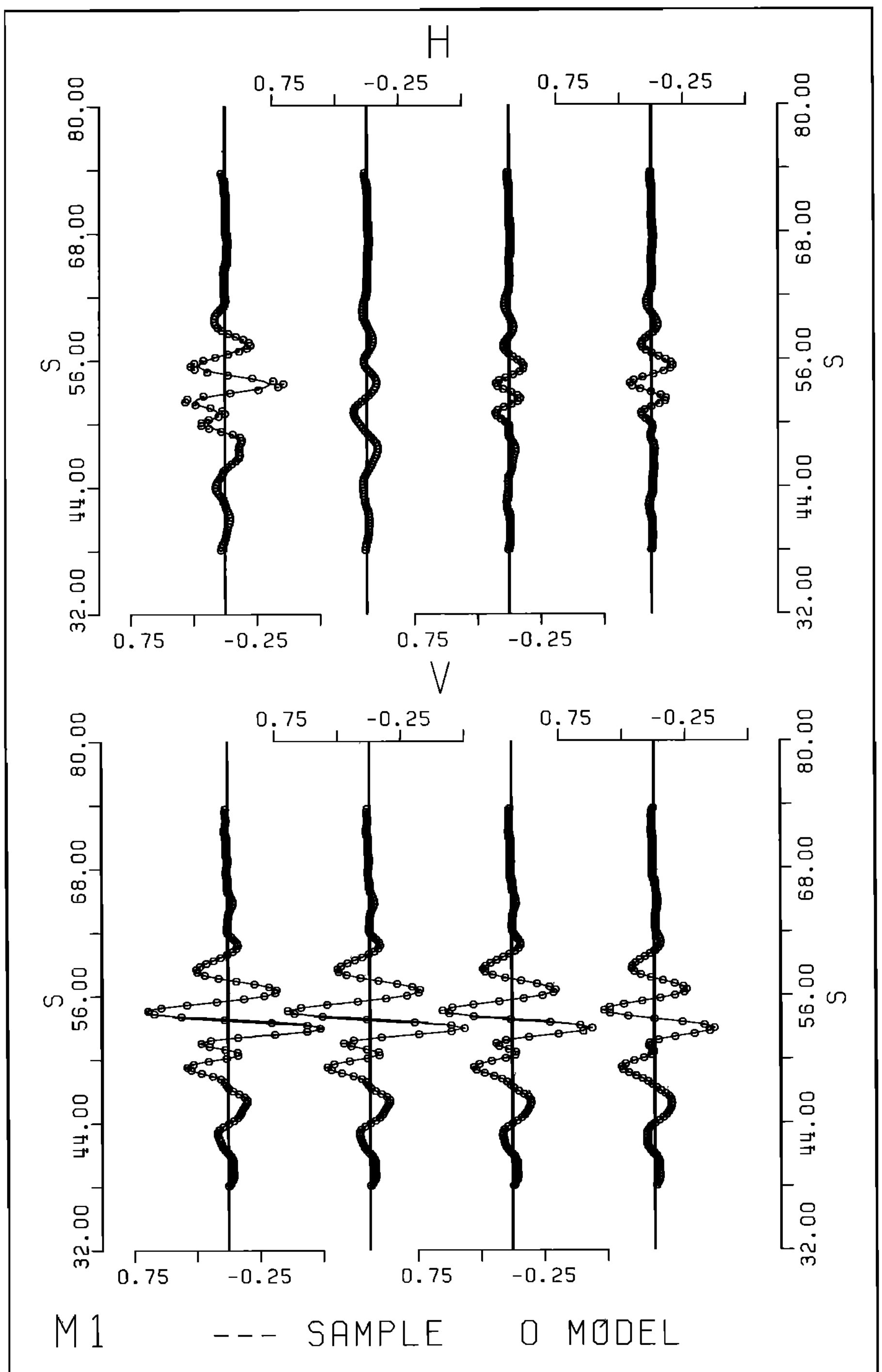

Fig. 5c. Model M1. Seismograms at the sensor array. Comparison between "observational" seismograms and model seismograms, represented by a continuous line (replacing the crosses of the preceding Figure) and by open circles, respectively. For legend, see Figure 5a.

contrasts with respect to the layer.

The concept of analysis consists in separating the wave transmitted across the basin into a (multimodal) Rayleigh wave and random noise. This means to focus attention on possible mode conversion, while nonmodal components, i.e., scattered leaky modes and body waves, are interpreted as background noise.

The modal wave component is modeled by the seismogram frequency spectra of the form

$$\begin{Bmatrix}\tilde{U}(x,z,\omega)\\ \tilde{W}(x,z,\omega)\end{Bmatrix} = \sum_n \begin{Bmatrix}\tilde{U}^{(n)}(x,z,\omega)\\ \tilde{W}^{(n)}(x,z,\omega)\end{Bmatrix}$$

$$= \sum_n \tilde{A}^{(n)}(\omega) \begin{Bmatrix}\tilde{T}_H^{(n)}(z,\omega)\\ \tilde{T}_V^{(n)}(z,\omega)\end{Bmatrix}$$

$$\cdot \exp(i\omega x/c^{(n)}) \qquad (8)$$

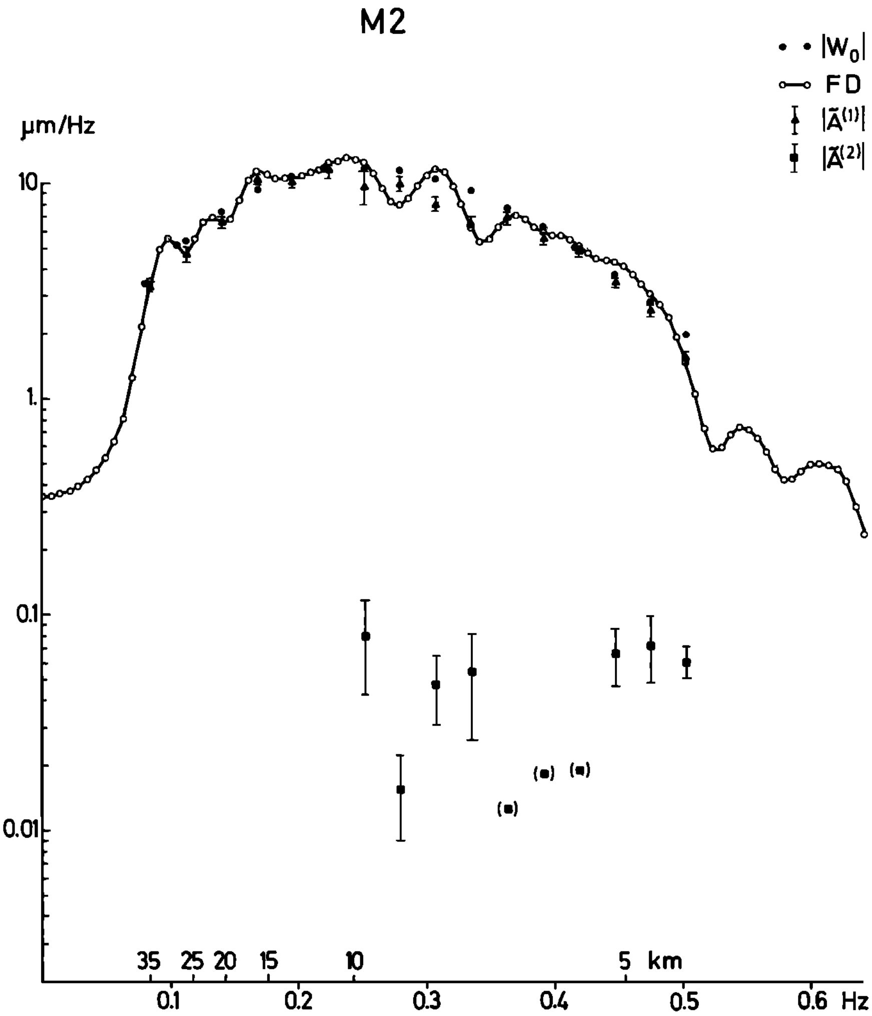

Fig. 6a. Model M2. Estimated mode coefficient amplitudes of the fundamental mode ($|\tilde{A}^{(1)}|$) and of the first higher mode ($|\tilde{A}^{(2)}|$), with 95% confidence intervals. Bracketed symbols refer to statistically insignificant estimates. The estimates are compared to the vertical component surface amplitude spectra of the incident fundamental mode ($|W_0|$) and of the transmitted wave at the sensor array (FD), respectively.

(see (1) and (5)), where $\tilde{A}^{(n)}(\omega)$ is generally not equal to $A^{(1)}(\omega)$, due to the influence of the basin.

The mode structure of the wave transmitted is determined from a number of seismograms "observed" at a hypothetical sensor array located beyond the basin. With respect to the seismogram frequency spectra, the concept of analysis implies that

$$V_i(x,z,\omega) = \tilde{V}_i(x,z,\omega) + e_i^!(x,z,\omega) \qquad i=1,\ldots,2\ell \tag{9a}$$

where V_i stands for $\{U_k, W_k\}$ $k=1,\ldots,\ell$ representing a set of complex observational spectrum samples; $\tilde{V}_i$ stands for the corresponding set $\{\tilde{U}_k, \tilde{W}_k\}$; and $e_i^!$ represents the spectral density of a random "residual process."

By a priori assumption,

$$E(e_i^!) = 0 \qquad i=1,\ldots,2\ell \tag{9b}$$

The assumption actually applies to the residuals arising at each of the sensor locations separately.

Hence the mode structure is obtained by least-squares fitting between model spectra ($\tilde{V}_i$) and observational spectra (V_i). The discrete linear inverse problem is equivalent to solving the system of equations

$$V_i(x,z,\omega) = \sum_{j=1}^{m} L_{ij}(x,z,\omega,n)\, \tilde{A}_j(\omega,n) \qquad i=1,\ldots,2\ell \qquad 2\ell > m \tag{10}$$

where the right-hand side stands for the model representation of (8); L_{ij} denotes the product between vertical and horizontal transfer function, and $\tilde{A}_j$ denotes the (generally complex) mode coefficient to be estimated.

In real matrix notation, the system (10) is weighted by multiplication with a diagonal matrix containing the inverse observational spectra, and solved by the generalized matrix inverse [for example, Searle, 1971].

Estimation Statistics

Use of the generalized inverse matrix in solving the linear equations (10) involves a

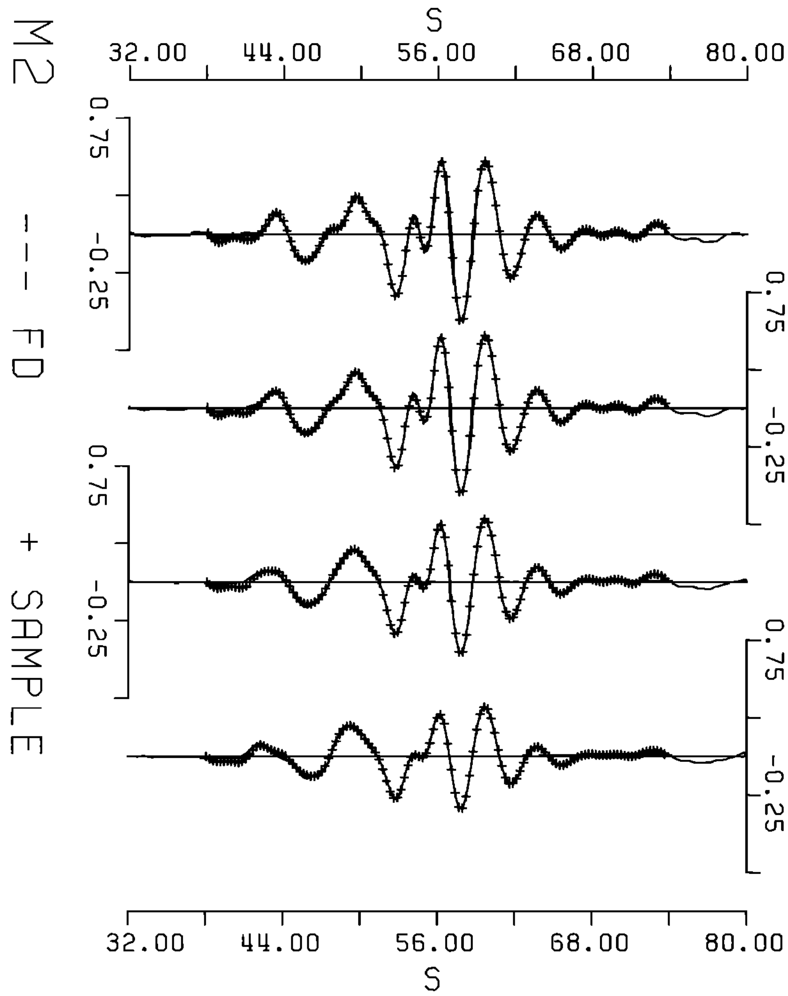

Fig. 6b. Model M2. Vertical component seismograms at the sensor array, corresponding to increasing depth from top to bottom. Comparison between FD seismograms and observational seismograms, represented by a continuous line and by crosses, respectively.

"singular value decomposition" of the weighted rectangular matrix (L_{ij}). For the models considered, the matrix proves to be well-conditioned; therefore the matrix inverse is constructed by inclusion of all singular values and their eigenvectors. The corresponding resolution matrix is an identity matrix, i.e., the solution is unique.

On the premise of independent residuals normally distributed about zero, a $100(1-\alpha)$ percent confidence interval associated with the unbiased estimate $\tilde{A}_j$ is given by

$$d_j = 2\, t_{2\ell-m}(\alpha/2)\, \sqrt{\mathrm{var}(\tilde{A}_j)} \tag{11}$$

The equation applies to real and imaginary parts separately; the radical is the variance of the estimate, and $t_{2\ell-m}(\alpha/2)$ represents the 100α percentage point of the t-distribution on $2\ell-m$ degrees of freedom. An estimate $\tilde{A}_j$ is considered significant when real and imaginary parts of the estimate exceed the confidence interval halfwidth.

A measure of the goodness-of-fit of the model is given by the coefficient of determination between V_i and $\tilde{V}_i$:

$$R^2 = 1 - \frac{1}{4\ell} \sum_{i=1}^{2\ell} |e_i|^2 \tag{12}$$

Physically, $e_i = e_i'/V_i = 1 - \tilde{V}_i/V_i$ represents the residual spectral density normalized by the observed spectral density (see (9a)). Hence the quantity $1 - R^2$ is related to the average power of the normalized residual process, and may serve as an indicator of the power of nonmodal noise.

Laterally Homogeneous Model

The "incident" fundamental Rayleigh mode is defined in terms of a Ricker pulse (Figure 1) representing the vertical component seismogram at the coordinate origin. The pulse amplitude spectrum is given in Figure 2.

To test the method of investigation, the wave is propagated across the undisturbed waveguide (model M1) consisting of a layer of sedimentary

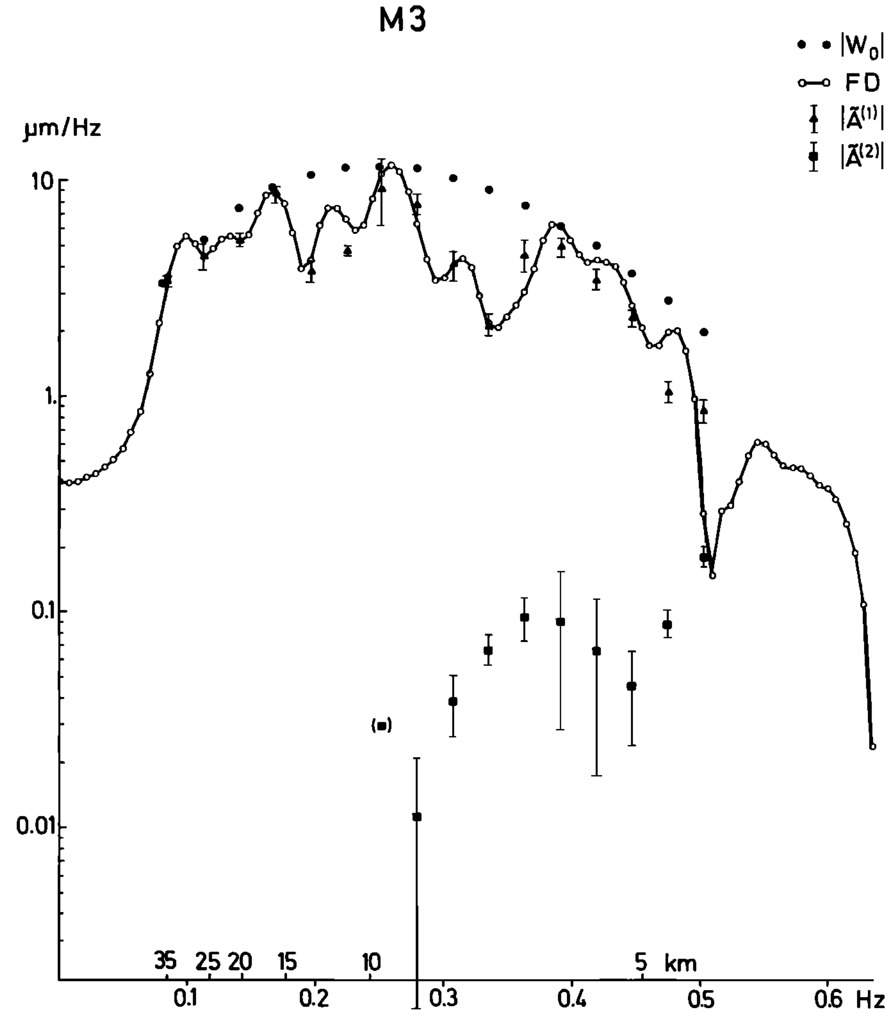

Fig. 7a. Model M3. For legend, see Figure 6a.

rock velocity of 5 km thickness over a homogeneous substratum of crystalline rock velocity. Theoretically, the fundamental mode displacements occupy a large space. For the purpose of FD wave propagation, the displacements are defined to be zero outside a range extending 60 km laterally and 20 km downward. Hereby, amplitudes of modulus lower than 0.5% and 5% of the maximum amplitude are neglected in the lateral and downward direction, respectively. This wave propagated numerically is compared to the analytical wave propagated by phase shifting.

Figure 2 compares phase velocity estimated from two FD surface seismograms, to theoretical phase velocity. Numerical and theoretical results closely agree in a limited frequency band, while outside this band, there are rapidly increasing deviations. As a consequence, interpretation is confined to the interval 0.08-0.50 Hz defined as "analysis interval." (This will be valid for all of the models considered.) Fundamental mode wavelengths of the analysis interval cover a range of 5 to 35 km, the wavelength of maximal spectrum amplitude being 10 km.

The wave propagated is recorded by an array of hypothetical sensors distributed vertically at four locations with 1 km spacing, at a horizontal distance of 110 km from the coordinate origin (Figure 1). Inversion is based upon the seismogram spectra sampled at 16 equidistant frequencies (separated by about 0.03 Hz) of the analysis interval, yielding a total of 64 complex spectral values per component of motion--defined as "observations."

Now, the analysis interval implies no more than the two lowest modes. Sampling at the frequencies defined, of the trapped modes which are characterized by zero energy below cut-off, yields a total of 26 generally complex mode coefficients to be determined in the inversion. Hence the number of observations is about 2.5 times the number of unknowns.

Figures 3a and 3b show the array seismogram spectra obtained numerically, in relation to those obtained theoretically. The componental spectra are compared in terms of amplitude and phase at the sample frequencies of the analysis interval. According to Figure 3a, the amplitudes differ by about maximally 15% in the case of the vertical component, whereas considerably larger

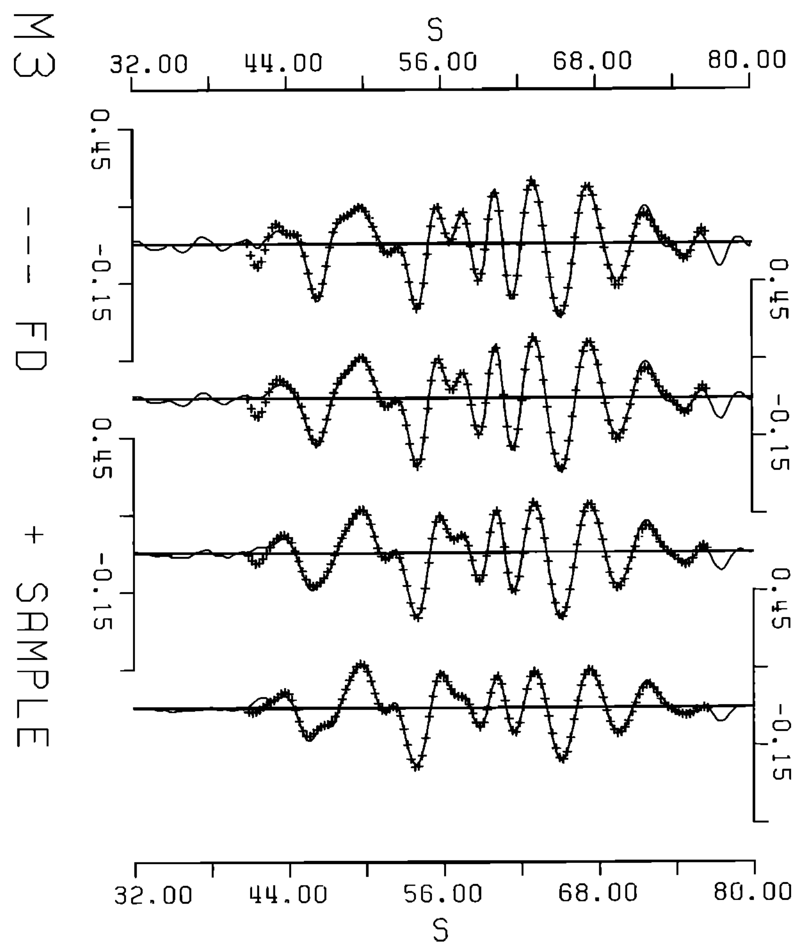

Fig. 7b. Model M3. For legend, see Figure 6b.

deviations occur in the case of the horizontal component.

According to Figure 3b, the phase difference is nearly independent of the depths considered for the vertical component. The increase of phase delay with frequency--a well-known feature of grid dispersion--is given approximately by a quadratic law, $\Delta\Phi(f) = -\gamma(f-f_0)^2$, where f denotes frequency (Hz), and $f_0 = 0.1$ (Hz), and $\gamma = 8$ (degrees times seconds squared). For the horizontal component, a corresponding trend in phase delay is obvious, although there are distinct variations between individual depths.

In the case of the horizontal component, both amplitude and phase deviate considerably from the average trend at 1 km and, to a smaller degree, at 2 km depth. Actually, near these depths, the sense of polarization of the fundamental mode motion reverses, implying a node of the horizontal component. This means that a small bias of the FD wave may be responsible for a change in sign of the phase, as well as a large relative deviation of the amplitude.

To find out the implications in the inversion, the wave propagated numerically has been inverted using the spectra of both horizontal and vertical components, on the one hand, and the spectra of the vertical component only, on the other hand. Compared to the former approach, the latter leads to mode coefficient estimates which agree better with theory. Also, the latter approach results in a much smaller spread and a higher degree of symmetry of the distribution of residuals (Figure 4a). Inferred from the coefficient of determination, the model accounts for 99% of the observations in the latter approach, compared to 84% in the former approach. For illustrative purposes, Figures 5a-5c compare theoretical seismograms, FD seismograms, "observational" seismograms corresponding to the sampled spectra of the FD seismograms, and model seismograms computed from the mode coefficient estimates resulting from inversion of the vertical component observational spectra. Note that observational seismograms and model seismograms are based upon the sample frequencies of the analysis interval. Owing to the sampling rate (as defined above) the corresponding seismograms have a length of 36 s; outside this interval they are repeated periodically by definition of the fast Fourier transform (FFT) applied.

Figure 5a compares FD seismograms and theoretical seismograms at the recording array. There is good agreement in general. Deviations of the long period components occurring before about 50 s, seem to result from the restricted vertical extent of the numerical grid. The horizontal component well illustrates the change in polarization close to 1 km depth. Figure 5b compares observational seismograms and FD seismograms. Their close agreement demonstrates

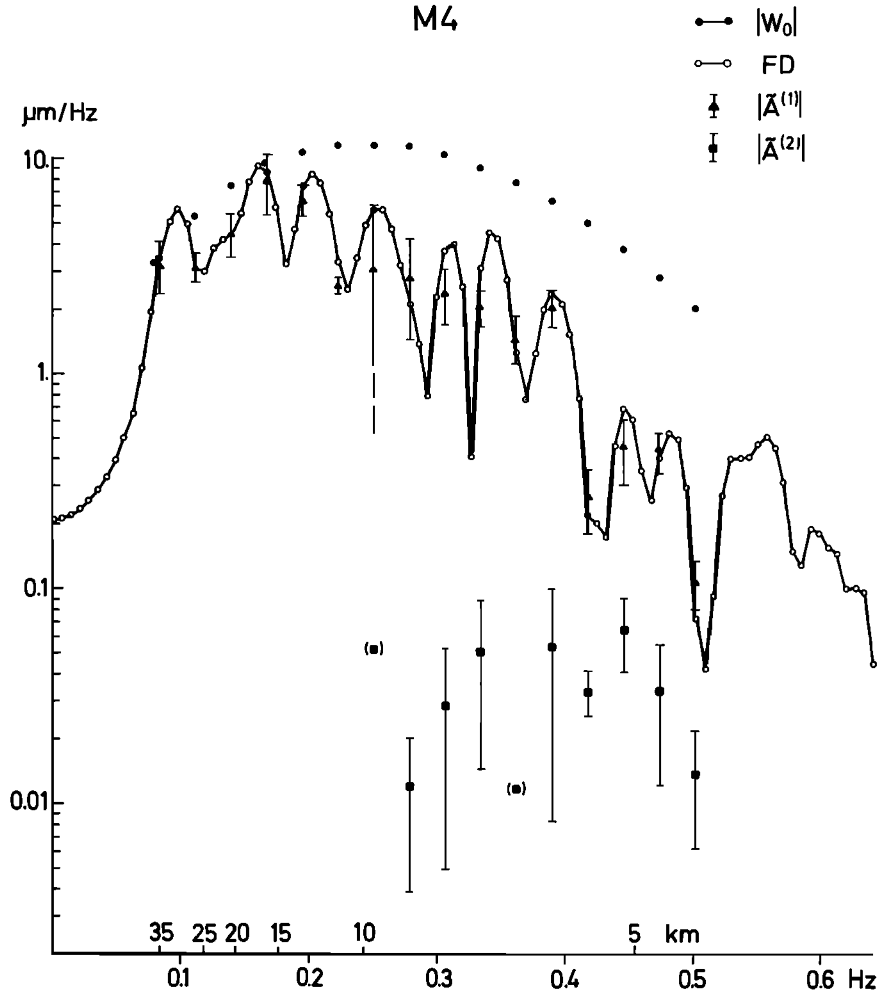

Fig. 8a. Model M4. For legend, see Figure 6a.

adequate sampling rate. Figure 5c compares model seismograms and observational seismograms. Their close agreement demonstrates close model fit.

Laterally Heterogeneous Models

In the following, the layered model includes a local heterogeneity of the form of a rectangular basin at the surface (Figure 1). While the basin geometry is kept constant, the elastic parameters of the basin are varied to obtain different velocity (or impedance) contrasts with respect to the layer. The incident fundamental Rayleigh mode described analytically occupies the space to the left of the basin. The wave is transmitted across the basin by FD approximation, and recorded at the vertical array of sensors situated 70 km--being double the maximum wavelength of the analysis interval--beyond the basin. In view of the results for the undisturbed waveguide, the inversion is based upon the vertical component seismogram spectra only.

Three models are considered. The basin properties correspond to low velocity sedimentary rocks for two models, and to vacuum for one model. The models are characterized by a shear wave velocity ratio between the basin and the layer, of 0.6 (model M2), 0.4 (model M3), and 0.0 (model M4), respectively. Consistent with the previous assumption, the residuals produced by the fitting procedure prove to be almost normally distributed about zero for all models (Figure 4b). Thus (11) and (12) provide meaningful criteria for the estimates and the total model.

Figures 6a, 7a, and 8a give the estimated mode coefficient amplitudes, along with their associated 95% confidence intervals. Also, the figures show the amplitude spectra of surface seismograms representing the wave transmitted across the basin, and the incident wave or, equivalently, the wave transmitted across the undisturbed waveguide. Comparing the wave transmitted (across the basin) to the incident wave in terms of the amplitude spectral density, the following is evident (only the analysis interval is considered). In the case of model M2, the wave transmitted is modified negligibly, except for small but significant reductions at about 0.3 Hz. In the case of model M3, over most of the frequency interval, the wave transmitted is reduced such that frequency bands of distinct reduction alternate with bands of low reduction. In the case of model M4, the wave transmitted is reduced substantially at all frequencies from about 0.2 Hz upward, and exhibits strong variations with frequency.

The estimated mode coefficients have statis-

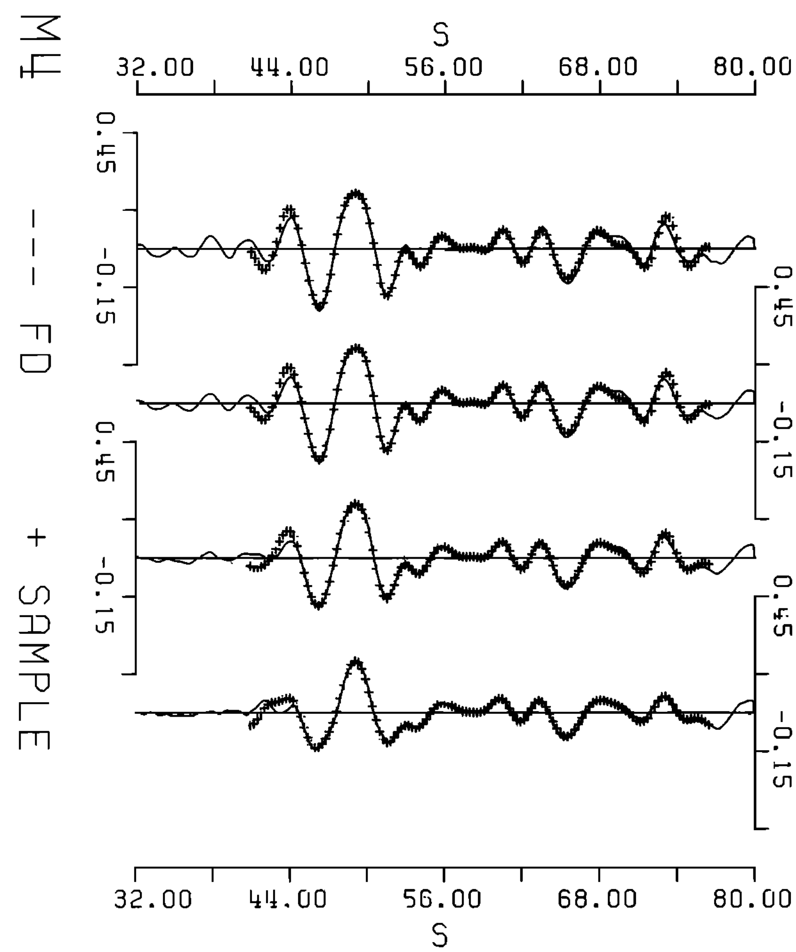

Fig. 8b. Model M4. For legend, see Figure 6b.

tically significant amplitudes for the fundamental mode and also for the first higher mode. The higher mode contribution is relatively small in the case of model M2, and tends to increase with increased velocity contrast. This aspect will be discussed in more detail below.

Figures 6b, 7b, and 8b show the seismograms at the sensor array, for the models considered. The figures compare the FD seismograms to the observational seismograms, demonstrating that the FD seismograms are accurately reproduced by the sampling of their spectra. In comparison with model M1 (Figure 5b), the seismograms are diminished in amplitude and extended in time. The effect is moderate in the case of model M2, and becomes more pronounced for the models of higher velocity contrast. Apparently, the seismograms are affected mainly at times from about 50 s onward; this implies a relatively small influence of the basin upon the high velocity components which correspond to the long wavelength components.

The model seismograms (not shown) computed from the mode coefficient estimates, are nearly identical to the observational seismograms, due to a close model fit in all of the cases.

Mode Conversion

In terms of the mode coefficient amplitudes, higher Rayleigh mode excitation appears to be relatively unimportant. This is in contrast to results from an earlier paper dealing with Love wave transmission across a basin type heterogeneity [Szelwis, 1983]. That paper considers two models resembling M2 and M3. For both models, the mode coefficient amplitudes of the higher mode are comparable to those of the fundamental mode.

To enable more direct comparison between the two waves, Love wave transmission is reinvestigated for the subsurface models considered in the present paper. The incident fundamental Love mode is defined by the amplitude spectrum corresponding to the vertical component fundamental Rayleigh mode. This implies similar wave-

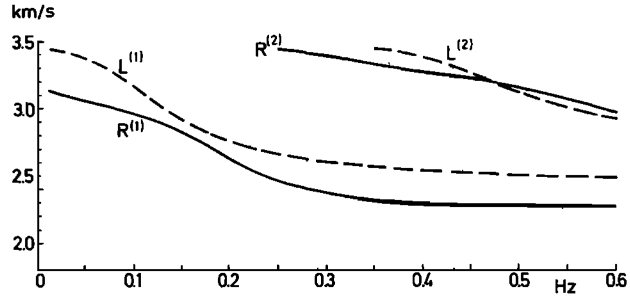

Fig. 9. Model M1. Modal phase velocity of Rayleigh waves (R) and Love waves (L).

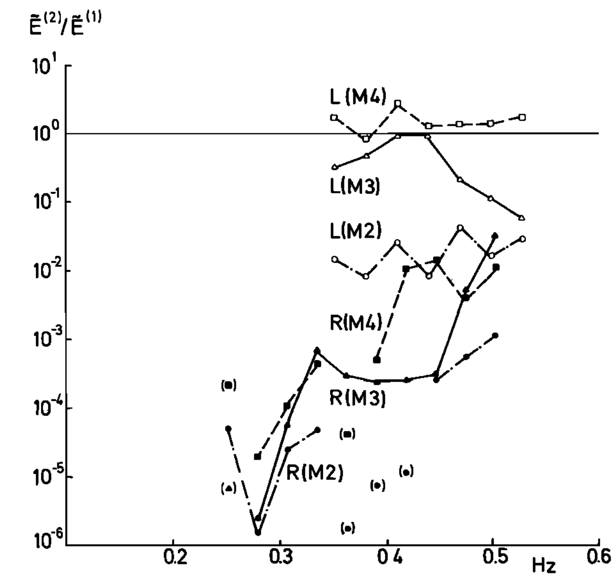

Fig. 10. Energy ratio between the first higher mode and the fundamental mode transmitted. Comparison between Rayleigh and Love waves for the laterally heterogeneous models.

lengths, owing to relatively close phase velocities of the undisturbed layer model (Figure 9).

The mode coefficient amplitudes are related to the rate of modal energy transport per unit width of the wavefront:

$$\tilde{E}^{(n)}(\omega) = \frac{1}{2}\,\omega\, k^{(n)} |\tilde{A}^{(n)}|^2 \qquad (13)$$

[Lysmer and Drake, 1972].

Figure 10 gives the ratio $\tilde{E}^{(2)}/\tilde{E}^{(1)}$ for Rayleigh and Love waves. The two waves consistently exhibit increasing mode conversion with increased velocity contrast. They differ in the relative amount of first higher mode energy, which is less by orders of magnitude, and also shows a more pronounced frequency dependence for the Rayleigh wave compared to the Love wave.

Field experiments generally do not provide coordinate-independent mode energy, but rather modal amplitudes involving the subsurface transfer functions. For comparison between the two waves, the amplitude spectral density of a Rayleigh mode is defined here by

$$\begin{aligned} \tilde{\sigma}^{(n)}(x,z,\omega) &= (|\tilde{U}^{(n)}|^2 + |\tilde{W}^{(n)}|^2)^{1/2} \\ &= |\tilde{A}^{(n)}|(|\tilde{T}_H^{(n)}|^2 + |\tilde{T}_V^{(n)}|^2)^{1/2} \\ &\equiv |\tilde{A}^{(n)}|\; T_{eff}^{(n)} \end{aligned} \qquad (14)$$

(see (8)).

In the case of Love modes, the "effective transfer function" $T_{eff}^{(n)}$ is replaced by the magnitude of the (scalar) Love mode transfer function.

Figures 11a-11c show the amplitude spectral density of Love and Rayleigh modes at the surface. The figures reflect a decrease of the transmitted wave relative to the incident wave, and also an increase of the first higher mode contribution relative to the fundamental mode contribution, parallel to increased velocity contrast. Remarkably, both Love and Rayleigh waves display higher mode contributions of the order of the fundamental mode contributions.

In the following, the role of the subsurface transfer functions in the depth range of the

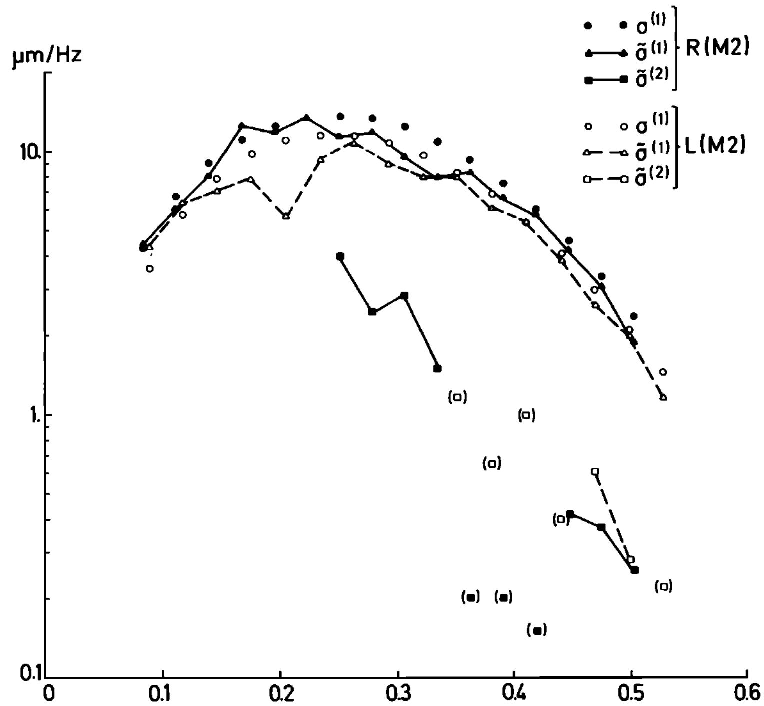

Fig. 11a. Model M2. Modal amplitude spectra at the surface. Comparison between Rayleigh and Love waves in terms of the incident mode ($\sigma^{(1)}$) and the transmitted modes at the sensor array ($\tilde{\sigma}^{(1)}$, $\tilde{\sigma}^{(2)}$).

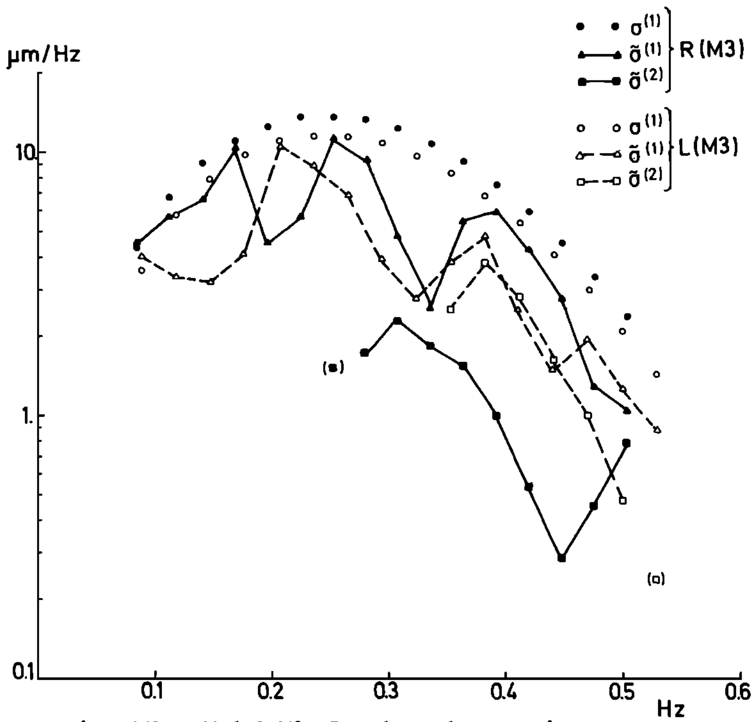

Fig. 11b. Model M3. For legend, see Figure 11a.

sensor array is considered. Figures 12a and 12b show the magnitude of the first higher mode transfer function divided by the fundamental mode transfer function for model M1. In the case of the Love wave (Figure 12a), the ratio is almost frequency independent, decreasing from unity at the surface toward zero at a depth of 2 to 2.5 km, then increasing with depth. Figure 12b shows the ratio of the effective Rayleigh mode transfer functions as defined by (14). At low frequencies, the ratio takes on relatively high values increasing with depth from about 100 at the surface

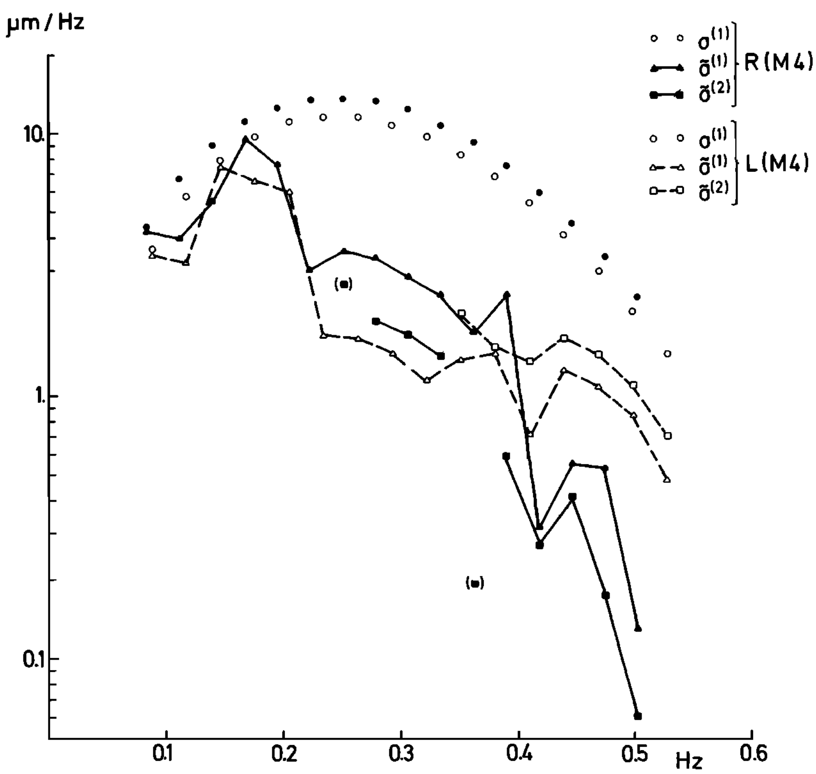

Fig. 11c. Model M4. For legend, see Figure 11a.

to about 200 near the depth of the bottom sensor. With increasing frequency, the ratio decreases toward about unity at the surface, and to about 10 at the depth of the bottom sensor.

Comparing the ratio of modal transfer functions to the ratio of modal energies (Figure 10), the following is evident. A high energy ratio corresponds to a low ratio of the transfer functions, and vice versa. This relation basically accounts for the discrepancy between the modal energies of Rayleigh and Love waves. It must be noted that the transfer functions are nonunique, hence this also applies to the mode coefficients, respectively the mode energy.

In terms of mode amplitudes defined by the product of mode coefficient and transfer function, Rayleigh and Love waves are roughly comparable (Figures 11a-11c). Accordingly, mode conversion is relevant for both waves. An aspect important for applications is that the presence of several modes in the wave transmitted across the basin, gives rise to modulation in the horizontal direction of the wave amplitude spectrum.

Energy Balance

The influence of the basin is now considered in terms of the fraction of transmitted energy. From (13) it follows that

$$E_A = \frac{\omega}{2} k^{(1)} |W_0|^2$$
$$\tilde{E} = \frac{\omega}{2} \sum_{n=1}^{2} k^{(n)} |\tilde{A}^{(n)}|^2 \qquad (15)$$

represent the energy of the incident fundamental mode and of the modal field transmitted, respectively; W_0 denotes the Fourier spectrum of the Ricker pulse representing the seismogram at the coordinate origin, of the Love wave, or of the vertical component Rayleigh wave.

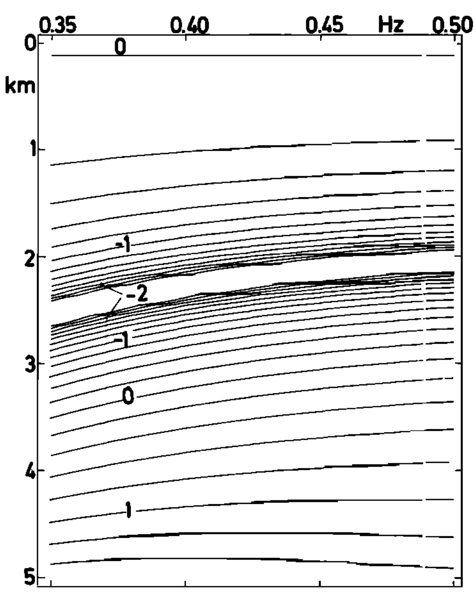

Fig. 12a. Model M1. Contour plot of log($|T_L^{(2)}/T_L^{(1)}|$), where $T_L^{(n)}$ is the transfer function of the n-th Love mode. Coordinates are frequency and depth. The contour spacing is 0.2.

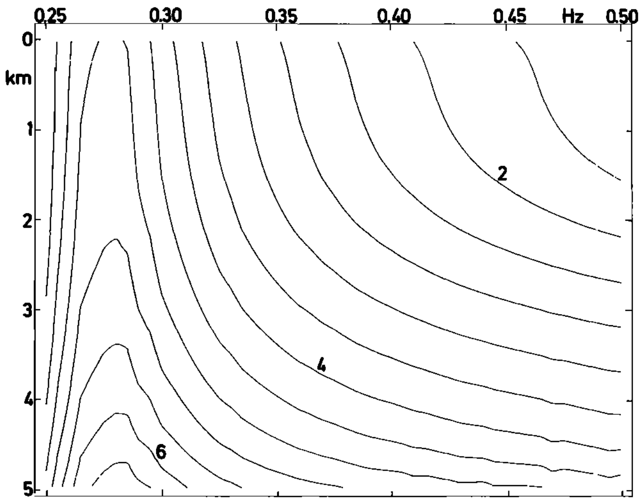

Fig. 12b. Model M1. Contour plot of log($T_{eff}^{(2)}/T_{eff}^{(1)}$), where $T_{eff}^{(n)}$ is the "effective" transfer function of the n-th Rayleigh mode. The contour spacing is 0.4.

Figure 13 gives $\tilde{E}/E_A$ for Rayleigh and Love waves. The two waves resemble in magnitude and frequency dependence. As indicated by the amplitude spectral density, the energy spectrum of the incident mode is distorted increasingly with increased velocity contrast. Minimal values of the fraction of transmitted modal energy are of the order of 50% for model M2, 10% for model M3, and 1% for model M4.

An estimate of the fraction of total modal energy transmitted is obtained by the ratio

$$\tilde{F}/F_A = \sum_{\omega} \tilde{E}(\omega) \; / \; \sum_{\omega} E_A(\omega) \qquad (16)$$

where summation is over the sample frequencies of the analysis interval.

The ratio is given in Table 1 for Rayleigh and Love waves. It proves a sensitive indicator of the velocity contrast, almost agreeing for the two waves.

Table 1 also gives the quantity $1-R^2$ related to the residuals of the fitting procedure (see (12)), which serves as a coarse measure of the fractional power of nonmodal noise in the transmitted wave. The difference between the two waves suggests that losses due to (forward) scattering into nonmodal components, are more important for the Love wave compared to the Rayleigh wave. Generally, the fraction of noise in the wave transmitted is small; therefore the energy deficit between the modal wave transmitted and the incident wave must be attributed essentially to reflection at the basin.

(Note: The influence of a water basin upon a Love wave corresponds with the influence of a vacuum basin. The influence of a water basin upon a Rayleigh wave is difficult to evaluate, due to instability of the heterogeneous FD approximation at a fluid-solid interface. Alternatively, if use is made of the explicit formulation of the boundary conditions for a solid-solid interface, where the shear wave velocity is assumed zero for the fluid, a stable FD scheme is obtained. The scheme implies continu-

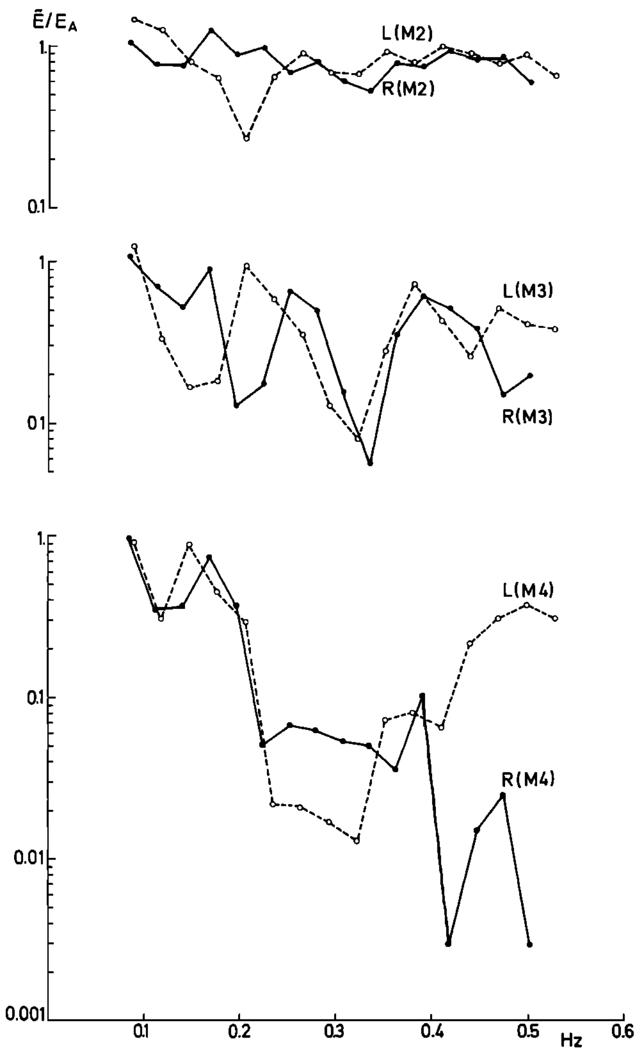

Fig. 13. Energy ratio between the modal component transmitted and the incident mode. Comparison between Rayleigh and Love waves for the laterally heterogeneous models.

ity of the component of motion parallel to the boundary, and hence violates the physical slip condition. For the model configuration of this paper, the corresponding bias appears to be small. By making use of that approach in analyzing the water basin model, it follows that there is some analogy to the vacuum basin model; for example, the ratio $\tilde{F}/F_A$ is given by 0.10, and the quantity $1-R^2$ by 0.07. On the other hand, there are nonnegligible differences concerning the mode structure and the spectral representation of $\tilde{E}/E_A$.)

Concluding Remarks

The hybrid method of analysis is affected by errors due to the FD approximation, the sampling approximation, and the fitting procedure.

1. The FD approximation has been investigated by comparison with theory for the case of the undisturbed layering. This has led to the definition of an "analysis interval" where numerical errors are minimal. In the case of the basin, the accuracy of the FD scheme is somewhat uncertain. First, the heterogeneous FD formulation involves a continuous approximation to the discontinuous change of Lamé's parameters at the basin boundaries. Second, FD results are biased increasingly with increased values of Poisson's ratio characterizing an elastic medium. The basin elastic parameters of models M2 and M3 imply a Poisson's ratio of 0.33 which is not considered a critically high value. In summary, FD propagation across the basin appears to be sufficiently accurate.

2. The sampling approximation implies the limited analysis interval and the sampling rate. The interval length does not affect the relative energy considered (although almost the entire wave energy is concentrated in the analysis interval). The sampling rate is adequate to reproduce the variations of the amplitude spectra in the case of models M2 and M3; whereas, in the case of model M4, it is relatively coarse leading to a smoothed version of the amplitude spectra.

3. The errors of the fitting procedure, i.e., the residuals, are related to the model of analysis. In the concept of this study, the sum of squares of the residuals yields a measure of nonmodal noise.

This study has provided quantitative evidence of surface wave transmission across a heterogeneity having dimensions of the order of the wavelengths. Fundamental mode Rayleigh and Love waves have been propagated numerically across a basin representing different velocity contrasts, and analyzed subsequently in terms of modes contaminated by nonmodal noise. It has been found that wave interaction with the basin gives rise to mode conversion which is increasingly important with increased velocity contrast. With regard to mode amplitudes conventionally considered in practice, the first higher mode contribution (due to mode conversion) is vastly comparable to the fundamental mode contribution, for both Love and Rayleigh waves transmitted. This implies that

TABLE 1. Laterally Heterogeneous Models

Model	ρ_3, g/cm^3	α_3, km/s	β_3, km/s	$(\tilde{F}/F_A)_R$	$(1-R^2)_R$	$(\tilde{F}/F_A)_L$	$(1-R^2)_L$
M2	2.2	3.0	1.5	0.77	0.01	0.76	0.12
M3	2.0	2.0	1.0	0.36	0.02	0.37	0.14
M4	0.0	0.0	0.0	0.09	0.06	0.11	0.12

Columns 2, 3, and 4 give the elastic parameters of the basin. Columns 5 and 6 refer to the Rayleigh wave, and columns 7 and 8 refer to the Love wave. For definition of symbols, see text.

the amplitude spectrum of the transmitted surface wave is modulated in the horizontal direction. The fraction of modal energy transmitted across the basin proves to be a sensitive indicator of the velocity contrast, and shows correspondence with respect to amount and frequency dependence between Rayleigh and Love waves.

Based upon two-dimensional models, the results of this paper may not simply be extrapolated to three-dimensional structures. However, it is demonstrated that variable sedimentary coverage, or a distinct topographic relief (or a water basin) may have significant influence upon surface waves of comparable wavelength scales.

Acknowledgment. The paper benefited greatly by critical comments to the manuscript.

References

Alford, R. M., K. R. Kelly., and D. M. Boore, Accuracy of finite-difference modeling of the acoustic wave equation, *Geophysics*, *39*, 834-842, 1974.

Boore, D. M., Finite-difference solutions to the equations of elastic wave propagation, with applications to Love waves over dipping interfaces, Ph.D. thesis, p. 240, Mass. Inst. of Technol., Cambridge, 1970.

Boore, D. M., Finite-difference methods for seismic wave propagation in heterogeneous materials, *Methods Comput. Phys.*, *2*, 1-36, 1972.

Bukchin, B. G., and A. L. Levshin, Propagation of Love waves across a vertical discontinuity, *Wave Motion*, *2*, 293-302, 1980.

Cheng, C. C., and B. J. Mitchell, Crustal Q structure in the United States from multi-mode surface waves, *Bull. Seismol. Soc. Am.*, *71*, 161-181, 1981.

Fuyuki, M., and Y. Matsumoto, Finite difference analysis of Rayleigh wave scattering at a trench, *Bull. Seismol. Soc. Am.*, *70*, 2051-2069, 1980.

Kelly, K. R., R. W. Ward, S. Treitel., and R. M. Alford, Synthetic seismograms: A finite-difference approach, *Geophysics*, *41*, 2-27, 1976.

Kijko, A., and B. J. Mitchell, Multimode Rayleigh wave attenuation and Q in the crust of the Barents Shelf, *J. Geophys. Res.*, *88*, 3315-3328, 1983.

Lysmer, J., and L. A. Drake, A finite element method for seismology, *Methods Comput. Phys.*, 11, 181-216, 1972.

Searle, S. R., *Linear Models*, p. 532, John Wiley, New York, 1971.

Szelwis, R., A hybrid approach to mode conversion, *Geophys. J. R. Astron. Soc.*, *74*, 887-904, 1983.

Tsai, Y. B., and K. Aki, Precise focal depth determination from amplitude spectra of surface waves, *J. Geophys. Res.*, *75*, 5729-5743, 1970.

R. Szelwis, Institut für Geophysik, Universität Hamburg, Bundesstr. 55, D-2000 Hamburg 13, Federal Republic of Germany.

(Received September 12, 1983;
revised April 5, 1984;
accepted August 15, 1984.)